Luo *et al.*
Chinese Journal of Mechanical Engineering (2023) 36:98
https://doi.org/10.1186/s10033-023-00928-z

Chinese Journal of Mechanical Engineering

ORIGINAL ARTICLE

Open Access

Source Quantitative Identification by Reference-Based Cubic Blind Deconvolution Algorithm

Xin Luo[1], Zhousuo Zhang[1*], Teng Gong[1] and Yongjie Li[1]

Abstract

The semi-blind deconvolution algorithm improves the separation accuracy by introducing reference information. However, the separation performance depends largely on the construction of reference signals. To improve the robustness of the semi-blind deconvolution algorithm to the reference signals and the convergence speed, the reference-based cubic blind deconvolution algorithm is proposed in this paper. The proposed algorithm can be combined with the contribution evaluation to provide trustworthy guidance for suppressing satellite micro-vibration. The normalized reference-based cubic contrast function is proposed and the validity of the new contrast function is theoretically proved. By deriving the optimal step size of gradient iteration under the new contrast function, we propose an efficient adaptive step optimization method. Furthermore, the contribution evaluation method based on vector projection is presented to implement the source contribution evaluation. Numerical simulation analysis is carried out to validate the availability and superiority of this method. Further tests given by the simulated satellite experiment and satellite ground experiment also confirm the effectiveness. The signals of control moment gyroscope and flywheel were extracted, respectively, and the contribution evaluation of vibration sources to the sensitive load area was realized. This research proposes a more accurate and robust algorithm for the source separation and provides an effective tool for the quantitative identification of the mechanical vibration sources.

Keywords Quantitative identification, Reference-based cubic contrast function, Semi-blind deconvolution, Satellite micro-vibration, Adaptive step size

1 Introduction

The micro-vibration of the sensitive load area is one of the key factors which affect the positioning accuracy and observation resolution of the satellite [1, 2]. The amplitude of the satellite micro-vibration is generally in the order of μm or even smaller. And its acceleration is generally in the order of mg. The micro-vibration with small amplitude does significant harm to satellite performance. The contribution proportions of the main sources to the sensitive load area obtained through the source quantitative identification can provide trustworthy guide for satellite micro-vibration suppression and possess great significance for improving satellite positioning accuracy, resolution and other performance.

The acquisition of pure source signals is one of the critical factors to accurately evaluate the contributions of the sources to the sensitive load area. However, the mixtures formed after mixing of multiple vibration sources rather than the source signals themselves are measured by the sensors. Therefore, extracting pure source signals from these mixtures is the basis for the smooth progress of source quantitative identification. The classical signal processing methods, such as variational mode decomposition (VMD) [3, 4], empirical mode decomposition

*Correspondence:
Zhousuo Zhang
zzs@mail.xjtu.edu.cn
[1] State Key Laboratory for Manufacturing Systems Engineering, Xi'an Jiaotong University, Xi'an 710049, China

(EMD) [5, 6] and wavelet transform (WT) [7, 8], have been proposed to acquire the source information from the mixture. It is to be regretted that these methods may fail in the satellite system, because the nonlinear characteristics caused by aluminum honeycomb sandwich panel and bolted connections will produce many harmonics, which increases the difficulty of source signals extraction.

Without prior information or with a small amount, Blind Source Separation (BSS) [9–11] possesses the ability for source separation only based on the mixed signals. It is extensively applied in acoustic signal processing [12, 13], biomedical signal processing [14, 15], communication system [16], image processing [17, 18] and mechanical systems [19, 20]. For complex mechanical systems, such as the satellite system, the mixing form of the multiple vibration signals is close to the convolutive mixing model. After years of research, many classical blind deconvolution algorithms have been proposed. By converting the convolutive mixing into the linear ones, the fast multi-channel blind deconvolution (MBD) algorithm is proposed by Thomas et al. [21]. Simon et al. [22] took higher-order cumulant as contrast function to realize the source signal extraction from the convolutive mixtures. In recent years, the semi-BSS algorithm improves the separation accuracy by introducing reference information, and has received considerable attentions. Castella et al. [23] introduced the reference signal into the higher-order cumulant and proposed the reference-based quadratic contrast function, which is effective on the i.i.d. and non-i.i.d. sources. In the framework of the reference-based quadratic contrast function, some optimization methods are proposed [24, 25]. On this basis, Dubroca et al. [26] proposed the reference-based cubic contrast function. The new contrast function shows less dependent on the reference signal, which provides great convenience for constructing the reference signal and improves the feasibility of the algorithm in practical application. As the optimization to the new contrast function, a general algebraic algorithm based on the best rank-1 tensor approximate is carried out. But this algebraic optimization method requires a good knowledge of the order of the filter due to its sensitivity on the rank estimation. Hence, Brahim et al. [27] proposed a new optimization algorithm which is based on a fixed step gradient and does not require any rank estimation. However, the fixed step optimization is time-consuming.

For the high-precision source extraction, the reference-based cubic blind deconvolution (RBCBD) algorithm is proposed. We first propose the normalized reference-based cubic contrast function and theoretically prove its validity. The new contrast function is then optimized by the adaptive step iteration, which does not require any rank estimation and which improves the efficiency. We also introduce the reference signal iterative updating and the deflation procedure to further improve the accuracy. Furthermore, the contribution evaluation method based on vector projection is presented to accurately evaluate the source contribution, so as to achieve the source quantitative identification. The validation of the proposed method is given by numerical simulation. The simulated satellite experiment constructed with reference to the real satellite was carried out to further verify this method. To confirm the effectiveness of the satellite micro-vibration source quantitative identification, the proposed method was applied to the satellite ground experiment to extract the signals of control moment gyroscope and flywheel and to compute the contribution proportions of the vibration sources to the sensitive load area.

The main structure of this paper is arranged below. The newly proposed RBCBD algorithm is introduced in Section 2. Contribution evaluation method based on vector projection is presented in Section 3. Section 4 gives the performance analysis of the source quantitative identification method through several numerical simulations. Then its availability is further confirmed by the simulated satellite experiment and satellite ground experiment in Section 5. Section 6 presents the conclusions.

2 Reference-Based Cubic Blind Deconvolution Algorithm

Extracting pure sources is the first step to obtain accurate source contribution, thus the RBCBD algorithm is proposed in this section to achieve efficient source extraction. Firstly, the blind deconvolution model is briefly introduced. Subsequently, the normalized reference-based cubic contrast function is presented. Finally, the novel contrast function is optimized through the adaptive step optimization method to realize the source extraction.

2.1 Blind Deconvolution Mathematical Model

For the N-dimensional unknown sources $\boldsymbol{s} = (s_1, s_2, \ldots, s_N)^{\mathrm{T}}$, the mathematical expression of their convolution mixing result is

$$\boldsymbol{x}(n) = \sum_{m\in\mathbb{Z}} \boldsymbol{A}(m)\boldsymbol{s}(n-m), \tag{1}$$

where the M-dimensional mixed signals $\boldsymbol{x} = (x_1, x_2, \ldots, x_M)^{\mathrm{T}}$ are collected by multiple sensors; $\boldsymbol{A}$ denotes the mixing matrix filter; M is the number of mixed signals; N is the number of source signals. It's commonly presumed that M is not less than N.

If the blind separation results are demanded to be closer to the expected one, some assumptions must be imposed on the unknown source signals and convolutive mixing system:

A1. $\boldsymbol{s}(n)$ are statistically independent.

A2. The mixing system is stable and invertible.

In the multi-input/single-output (MISO) context, the purpose of the blind deconvolution is to obtain the separation vector filter $\boldsymbol{w}$ and then the estimated source signal can be obtained by:

$$y(n) = \sum_{m\in\mathbb{Z}} \boldsymbol{w}(m)\boldsymbol{x}(n-m), \tag{2}$$

where $y(n)$ is an effective recovery of the source signal.

The global vector filter $\boldsymbol{g}(n)$ is defined as:

$$\boldsymbol{g}(n) \triangleq \sum_{m\in\mathbb{Z}} \boldsymbol{w}(m)\boldsymbol{A}(n-m). \tag{3}$$

Thus,

$$y(n) = (\boldsymbol{g} * \boldsymbol{s})(n) = \sum_{m\in\mathbb{Z}} \boldsymbol{g}(m)\boldsymbol{s}(n-m), \tag{4}$$

where $*$ is the symbol of the convolution operation.

Without prior information of any sources or the hybrid system, there exist some indeterminacies in the estimation results only through the observed signal. The extraction of the source signal can be achieved when the following condition is met:

$$\begin{aligned} &g_i(n) = \varepsilon(n)\delta_{i,i_0}, \\ &\exists i_0 \in \{1,\ldots,N\}, \forall i \in \{1,\ldots,N\}, \end{aligned} \tag{5}$$

where $g_i(n) \triangleq (\boldsymbol{g}(n))_i$ represents the ith element of the global vector filter; δ_{i,i_0} is the Kronnecker impulse function; ε is a non-zero impulse response filter.

Eq. (5) expresses that separated signal $y(n)$ is equivalent to a filtering of the source s_{i_0} by a impulse response filter $\varepsilon(n)$. Thus, the extracted signal is a filtered and permuted version of the source signal. These indeterminacies will not affect the contribution evaluation, which will be shown in the contribution evaluation section.

2.2 Normalized Reference-Based Cubic Contrast Function

One critical factor of blind separation is the contrast function. BSS can be considered as one optimization issue because maximizing or minimizing the appropriate contrast function can give an effective estimation of the source. Here, the general contrast function of BSS needs to meet the following properties:

P1.

$$\forall y(n) \in \mathbf{Y}, J\{y(n)\} \le \max_{i=1}^{N} \sup J\{(\varepsilon * s_i)(n)\}, \tag{6}$$

where $\mathbf{Y}$ denotes the set of output of Eq. (4).

P2. The equivalence in Eq. (6) holds if and only if $y(n)$ is a source filtered version obtained by the impulse response filter $\varepsilon(n)$, that is, when the global vector filter satisfies Eq. (5).

We present the normalized reference-based cubic contrast function as follows:

$$J(y) \triangleq \left| \frac{\mathrm{Cum}\{y(n), y(n), y(n), r(n)\}}{\mathrm{E}\left\{|y(n)|^2\right\}^{3/2}} \right|^2. \tag{7}$$

The reference signal $r(n)$ is presumed to satisfy the assumption below:

A3. $r(n)$ is obtained by filtering the source signal with a vector filter $\boldsymbol{h}(m)$:

$$r(n) = \sum_{m\in\mathbb{Z}} \boldsymbol{h}(m)\boldsymbol{s}(n-m). \tag{8}$$

Under assumptions A1, A2 and A3, J in Eq. (7) is a contrast function, i.e., J satisfies the properties P1 and P2. The proof is given below.

$C_r\{y(n)\} \triangleq \mathrm{Cum}\{y(n), y(n), y(n), r(n)\}$ denotes the reference-based cubic fourth-order cumulant.

Define $\bar{J}(y)$ by:

$$\bar{J}(y) \triangleq \frac{|C_r\{y(n)\}|}{\mathrm{E}\left\{|y(n)|^2\right\}^{3/2}}. \tag{9}$$

It is easy to know that the proof of J as the contrast function is equivalent to the proof of $\bar{J}$ as the contrast. Alternatively, the proof of $\bar{J}$ as contrast function will be made.

Firstly, the denominator part of Eq. (9) is analyzed. We define $\|g_i\|_i^2$ by:

$$\|g_i\|_i^2 \triangleq \sum_{(k_1,k_2)\in\mathbb{Z}^2} g_i(k_1)g_i(k_2)\mathrm{E}\{s_i(n)s_i(n-(k_2-k_1))\}. \tag{10}$$

Then we can get:

$$\mathrm{E}\left\{|y(n)|^2\right\} = \sum_{i=1}^{N} \|g_i\|_i^2, \tag{11}$$

and thus,

$$\mathrm{E}\left\{|y(n)|^2\right\}^{3/2} = \left(\sum_{i=1}^{N} \|g_i\|_i^2\right)^{3/2} \ge \sum_{i=1}^{N} \left(\|g_i\|_i^2\right)^{3/2} = \sum_{i=1}^{N} \|g_i\|_i^3. \tag{12}$$

Secondly, the numerator part $|C_r\{y(n)\}|$ of Eq. (9) is analyzed. Define $\bar{y}_i(n)$ by:

$$\bar{y}_i(n) \triangleq (\bar{g}_i * s_i)(n), \tag{13}$$

where

$$\bar{g}_i = \begin{cases} \frac{g_i}{\|g_i\|_i}, & \|g_i\|_i \neq 0, \\ \mathbf{0}, & \|g_i\|_i = 0. \end{cases} \tag{14}$$

Define $C_r^{\max}$ by:

$$C_r^{\max} \triangleq \max_{i=1}^{N} C_{r,i}, \tag{15}$$

where

$$C_{r,i} = \sup_{\|\bar{g}_i\|_i=1} \left| C_r\{(\bar{g}_i * s_i)(n)\} \right|. \tag{16}$$

Using the assumption A3, the mutual independence of signals $\bar{y}_i(n)$ and properties of cumulants, we have:

$$C_r\{y(n)\} = \sum_{i=1}^{N} \|g_i\|_i^3 C_r\{\bar{y}_i(n)\}, \tag{17}$$

thus,

$$\left| C_r\{y(n)\} \right| \leq \sum_{i=1}^{N} \|g_i\|_i^3 \left| C_r\{\bar{y}_i(n)\} \right| \leq C_r^{\max} \sum_{i=1}^{N} \|g_i\|_i^3. \tag{18}$$

Finally, using Eq. (12) and Eq. (18), we have:

$$\bar{J}(y) \triangleq \frac{\left| C_r\{y(n)\} \right|}{\mathrm{E}\left\{ |y(n)|^2 \right\}^{3/2}} \leq \frac{C_r^{\max} \sum_{i=1}^{N} \|g_i\|_i^3}{\mathrm{E}\left\{ |y(n)|^2 \right\}^{3/2}} \leq C_r^{\max}. \tag{19}$$

The above inequality proves the property P1 is satisfied. When equality is satisfied, we have:

$$\left(\sum_{i=1}^{N} \|g_i\|_i^2 \right)^{3/2} = \sum_{i=1}^{N} \left(\|g_i\|_i^2 \right)^{3/2}. \tag{20}$$

Then, at most one of $\|g_i\|_i^2$ is non-zero for all $i \in \{1, \cdots, N\}$. And $C_r^{\max} = C_{r,i}$ for this value of i. So far, the above derivation proves that property P2 can also be satisfied.

Therefore, we theoretically prove the validity of the normalized reference-based cubic contrast function.

In this section, we present the reference-based cubic contrast function, transforming the blind deconvolution problem into the optimization problem of maximizing the contrast function.

2.3 Optimization Method

2.3.1 Adaptive Step Size Gradient Optimization

We suppose that the separation vector filter $\boldsymbol{w}$ is a FIR filter with the filtering order D. The blind deconvolution model can be expressed by another form, that is, the ICA model:

$$y(n) = \underline{\boldsymbol{w}}\underline{\boldsymbol{x}}(n), \tag{21}$$

where

$$\underline{\boldsymbol{w}} = (\boldsymbol{w}(0), \boldsymbol{w}(1), \ldots, \boldsymbol{w}(D-1)), \tag{22}$$

$$\underline{\boldsymbol{x}}(n) = \left(\boldsymbol{x}(n)^{\mathrm{T}}, \boldsymbol{x}(n-1)^{\mathrm{T}}, \ldots, \boldsymbol{x}(n-D+1)^{\mathrm{T}} \right)^{\mathrm{T}}. \tag{23}$$

$\boldsymbol{R} \triangleq \mathrm{E}\{\underline{\boldsymbol{x}}(n)\underline{\boldsymbol{x}}(n)^{\mathrm{T}}\}$ is defined as the covariance matrix of the mixed signals, then we have $\mathrm{E}\left\{ |y(n)|^2 \right\} = \underline{\boldsymbol{w}}\boldsymbol{R}\underline{\boldsymbol{w}}^{\mathrm{T}}$. The contrast function J is a function of $\underline{\boldsymbol{w}}$:

$$J(\underline{\boldsymbol{w}}) = \bar{J}(\underline{\boldsymbol{w}})^2, \tag{24}$$

where

$$\bar{J}(\underline{\boldsymbol{w}}) \triangleq \frac{C_r\{\underline{\boldsymbol{w}}\underline{\boldsymbol{x}}\}}{(\underline{\boldsymbol{w}}\boldsymbol{R}\underline{\boldsymbol{w}}^{\mathrm{T}})^{3/2}}. \tag{25}$$

The iterative process with the gradient method is:

$$\underline{\boldsymbol{w}}(k+1) = \underline{\boldsymbol{w}}(k) + \mu \boldsymbol{d}, \tag{26}$$

where k is the iteration number; μ is the iterative step; and $\boldsymbol{d}$ represents the gradient of $J(\underline{\boldsymbol{w}})$, that is:

$$\boldsymbol{d} = \frac{\partial J(\underline{\boldsymbol{w}})}{\partial \underline{\boldsymbol{w}}} = 2\bar{J}(\underline{\boldsymbol{w}}) \frac{\partial \bar{J}(\underline{\boldsymbol{w}})}{\partial \underline{\boldsymbol{w}}}, \tag{27}$$

where

$$\frac{\partial \bar{J}(\underline{\boldsymbol{w}})}{\partial \underline{\boldsymbol{w}}} = \frac{\frac{\partial C_r\{\underline{\boldsymbol{w}}\underline{\boldsymbol{x}}\}}{\partial \underline{\boldsymbol{w}}} (\underline{\boldsymbol{w}}\boldsymbol{R}\underline{\boldsymbol{w}}^{\mathrm{T}})^{3/2} - 3C_r\{\underline{\boldsymbol{w}}\underline{\boldsymbol{x}}\}(\underline{\boldsymbol{w}}\boldsymbol{R}\underline{\boldsymbol{w}}^{\mathrm{T}})^{1/2}\underline{\boldsymbol{w}}\boldsymbol{R}}{(\underline{\boldsymbol{w}}\boldsymbol{R}\underline{\boldsymbol{w}}^{\mathrm{T}})^3}, \tag{28}$$

with

$$\frac{\partial C_r\{\underline{\boldsymbol{w}}\underline{\boldsymbol{x}}\}}{\partial \underline{\boldsymbol{w}}} = \frac{3}{N_e} (\underline{\boldsymbol{w}}\underline{\boldsymbol{x}})^2 \cdot r\underline{\boldsymbol{x}}^{\mathrm{T}} - \frac{3}{N_e^2} \left(2\underline{\boldsymbol{w}}\underline{\boldsymbol{x}} r^{\mathrm{T}} \underline{\boldsymbol{w}}\underline{\boldsymbol{x}}\underline{\boldsymbol{x}}^{\mathrm{T}} + \underline{\boldsymbol{w}}\underline{\boldsymbol{x}}\underline{\boldsymbol{x}}^{\mathrm{T}}\underline{\boldsymbol{w}}^{\mathrm{T}} r\underline{\boldsymbol{x}}^{\mathrm{T}} \right). \tag{29}$$

The convergence performance in terms of speed and accuracy will be directly influenced by the value of μ. As explained in Ref. [28]: A small μ will cause the algorithm slowly converge to the extreme point, while a large one will accelerate the convergence, also produce large steady-state error. To obtain $\underline{\boldsymbol{w}}$ rapidly and stably, it is expected that we can adaptively obtain the optimal value of μ to maximize the contrast function at every iteration, that is:

$$\mu_{adap} = \arg\max_{\mu} J(\underline{\boldsymbol{w}} + \mu \boldsymbol{d}). \tag{30}$$

The adaptive step size μ_{adap} is calculated below.

The derivative at the extreme point for a continuous function is 0, so the optimal step should meet that:

$$\frac{\partial J(\underline{\boldsymbol{w}}+\mu\boldsymbol{d})}{\partial\mu}=0. \tag{31}$$

Deduce the left side of Eq. (31), we have:

$$\frac{\partial J(\underline{\boldsymbol{w}}+\mu\boldsymbol{d})}{\partial\mu}=K(a_3\mu^3+a_2\mu^2+a_1\mu+a_0), \tag{32}$$

where K is a constant; and

$$\begin{aligned}
a_3&=(-\boldsymbol{np}\circ\boldsymbol{q}^2+\boldsymbol{lq}^3+\boldsymbol{n}^2\boldsymbol{p}-\boldsymbol{lnq})\boldsymbol{r}^{\mathrm{T}},\\
a_2&=(-2\boldsymbol{np}^2\circ\boldsymbol{q}+\boldsymbol{lp}\circ\boldsymbol{q}^2+\boldsymbol{mq}^3+3\boldsymbol{lnp}-2\boldsymbol{l}^2\boldsymbol{q}-\boldsymbol{mnq})\boldsymbol{r}^{\mathrm{T}},\\
a_1&=(-\boldsymbol{lp}^2\circ\boldsymbol{q}+2\boldsymbol{mp}\circ\boldsymbol{q}^2-\boldsymbol{np}^3+2\boldsymbol{l}^2\boldsymbol{p}+\boldsymbol{mnp}-3\boldsymbol{mlq})\boldsymbol{r}^{\mathrm{T}},\\
a_0&=(-\boldsymbol{lp}^3+\boldsymbol{mp}^2\cdot\boldsymbol{q}+\boldsymbol{mlp}-\boldsymbol{m}^2\boldsymbol{q})\boldsymbol{r}^{\mathrm{T}},
\end{aligned} \tag{33}$$

where $\circ$ is the symbol of Hadamard product; and

$$\begin{aligned}
\boldsymbol{p}&=\underline{\boldsymbol{w}}\underline{\boldsymbol{x}},\\
\boldsymbol{q}&=\boldsymbol{d}\underline{\boldsymbol{x}},\\
\boldsymbol{l}&=\underline{\boldsymbol{w}}\boldsymbol{R}\boldsymbol{d}^{\mathrm{T}},\\
\boldsymbol{m}&=\underline{\boldsymbol{w}}\boldsymbol{R}\underline{\boldsymbol{w}}^{\mathrm{T}},\\
\boldsymbol{n}&=\boldsymbol{d}\boldsymbol{R}\boldsymbol{d}^{\mathrm{T}}.
\end{aligned} \tag{34}$$

Constant K does not affect the solution. Then the real roots of the polynomial $p(\mu)=a_3\mu^3+a_2\mu^2+a_1\mu+a_0$ are the candidates of μ_{adap}. Substitute each candidate value into $J(\underline{\boldsymbol{w}}+\mu\boldsymbol{d})$, the candidate that maximize $J(\underline{\boldsymbol{w}}+\mu\boldsymbol{d})$ is the adaptive step size μ_{adap}. In each iteration, μ_{adap} is calculated first, which can significantly improve efficiency and ensure stability.

Owing to the inevitable scaling indeterminacy of BSS, the scale of the separation vector filter will not affect the separation performance. Hence, the constraint of unit-power $\mathrm{E}\{|y(n)|^2\}=1$ is common in BSS. This constraint is achieved by normalizing $\underline{\boldsymbol{w}}(k+1)$ after each iteration in the following form:

$$\underline{\boldsymbol{w}}(k+1)=\frac{\underline{\boldsymbol{w}}(k+1)}{\mathrm{E}\left\{\left|\underline{\boldsymbol{w}}(k+1)\underline{\boldsymbol{x}}(n)\right|^2\right\}^{1/2}}. \tag{35}$$

Repeat iteration until convergence, and the extraction of one source can be achieved by:

$$y(n)=\underline{\boldsymbol{w}}\underline{\boldsymbol{x}}(n). \tag{36}$$

The convergence can be judged by comparing the contrast function values before and after iteration.

Therefore, the steps of the single source signal extraction are as follows:

(1) Center the mixed signals $\boldsymbol{x}(n)$.
(2) Rewrite the mixed signals $\boldsymbol{x}(n)$ into its time-delay form $\underline{\boldsymbol{x}}(n)$.
(3) Initialize $\underline{\boldsymbol{w}}$ randomly and normalize it by Eq. (35).
(4) Calculate the gradient $\boldsymbol{d}$ by Eq. (27).
(5) Calculate the adaptive step size by Eq. (30).
(6) Iterate $\underline{\boldsymbol{w}}$ by $\underline{\boldsymbol{w}}(k+1)=\underline{\boldsymbol{w}}(k)+\mu_{adap}\boldsymbol{d}$.
(7) Normalize $\underline{\boldsymbol{w}}(k+1)$ by Eq. (35).
(8) If not convergence, go back to step (4).
(9) If convergence, extract the source signal by Eq. (36).

2.3.2 Optimization of Reference Signal Iterative Updating

An optimization method by iteratively updating reference signal [26] is introduced to further improve the separation accuracy.

The signal $y(n)$ extracted through the maximization of contrast function $J(\underline{\boldsymbol{w}})$ is more identical to the source $s_i(n)$ than the reference signal $r(n)$. Therefore, taking the extracted signal $y(n)$ as a new reference signal, we extract the source again by the proposed algorithm in Section 2.3.1. Then repeat the above operations several times. Single source signal extraction with the optimization method is carried out as follows:

(1) Construct the reference signal $r(n)$.
(2) Set $l=0$.
(3) Obtain the separation vector filter $\underline{\boldsymbol{w}}$ and the extracted signal $y(n)=\underline{\boldsymbol{w}}\underline{\boldsymbol{x}}(n)$ by the proposed algorithm in Section 2.3.1.
(4) Set $l=l+1$.
(5) If l does not reach the preset number of iterations, i.e., $l<l_{\mathrm{rs}}$, set $r(n)=y(n)$ and go back to step (3).
(6) If l reaches the preset number of iterations, i.e. $l\geq l_{\mathrm{rs}}$, the single source signal extraction is achieved.

2.4 Extraction of Multiple Source Signals

Let the mixed signals subtract the contribution of the previously extracted source signal, which can reduce separation difficulty and improve separation accuracy [29]. Wiener filter is taken to extract the source contribution. The parameters of the Wiener filter extracting the contributions of y_i in $\boldsymbol{x}$ can be solved by:

$$\boldsymbol{h}_i=\arg\min_{\boldsymbol{h}_i}\mathrm{E}\left\{\left\|\boldsymbol{x}-\boldsymbol{h}_i*y_i\right\|^2\right\}=\boldsymbol{R}_{xy_i}\boldsymbol{R}_{y_i}^{-1}, \tag{37}$$

where $\boldsymbol{R}_{xy_i}$ is an $(M\times L)$ matrix in which $\boldsymbol{R}_{xy_i}(u,v)=\mathrm{E}\{x_u(n)y_i(n-v+1)\}$; $\boldsymbol{R}_{y_i}$ is an $(L\times L)$ matrix in which $\boldsymbol{R}_{y_i}(u,v)=\mathrm{E}[y_i(n-v)y_i(n-u)]$; L is the Wiener filter length.

Then the contributions of y_i in $\boldsymbol{x}$ can be obtained by:

$$\hat{y}_i = (\hat{y}_{i1}, \ldots, \hat{y}_{iM})^{\mathrm{T}} = \boldsymbol{h}_i * y_i, \tag{38}$$

where $\hat{y}_{ij}$ denotes the contribution of y_i in x_j.

Replacing the original mixed signals $\boldsymbol{x}$ with the remaining mixed signals $\boldsymbol{x}_r = \boldsymbol{x} - \hat{\boldsymbol{y}}_i$ reduces the source number in the mixtures. Then continue the source extraction based on the remaining mixed signals. Repeat the extraction process until all estimated source signals $\boldsymbol{y} = (y_1, y_2, \ldots, y_N)^{\mathrm{T}}$ are obtained.

The flowchart of multiple source signals extraction is illustrated in Figure 1.

3 Contribution Evaluation Based on Vector Projection

Source quantitative identification includes source extraction and relative influence evaluation of the different sources on the observations. The contribution evaluation is an intuitive mathematical expression of this relative influence proportion. The contribution evaluation is usually based on signal energy [30, 31]. However, under the conditions of frequency-band overlap, the energy sum of each source contribution is not equal to the energy of the mixed signal, causing the energy-related contribution evaluation can't accurately express the true influence.

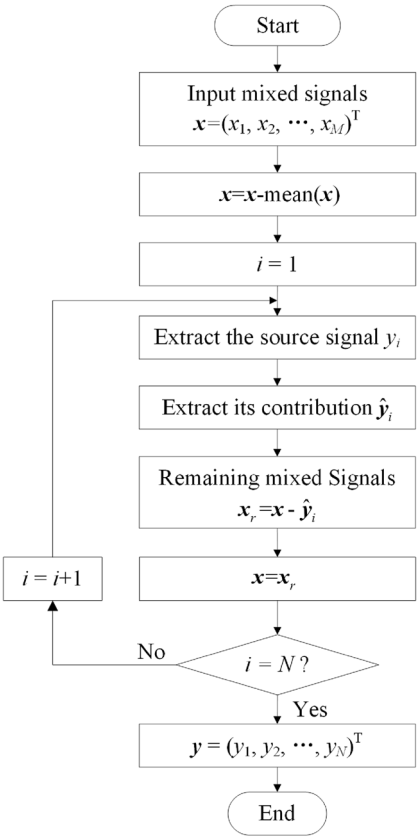

Figure 1 Flowchart of multiple source signals extraction

The contribution evaluation method based on vector projection is presented. By the form of vector inner product, the source contribution $\hat{y}_{ij}$ is projected on the mixed signal x_j as:

$$\hat{y}'_{ij} = \hat{y}_{ij} \cdot \frac{x_j}{\|x_j\|_2}, \tag{39}$$

where $\cdot$ represents the inner product operation; $\|\cdot\|_2$ denotes the 2-norm.

Then the contribution proportion (CP) of the ith extracted source y_i to the jth mixed observation x_j is expressed through the proportion of $\hat{y}'_{ij}$ in x_j:

$$\mathrm{CP}_{ij} = \frac{\hat{y}'_{ij}}{\|x_j\|_2} = \frac{\hat{y}_{ij} \cdot x_j}{x_j \cdot x_j}. \tag{40}$$

Easy to get that the mixed signal at one observation point is the sum of each source contributions at this point, that is

$$x_j = \sum_{i=1}^{N} \hat{y}_{ij}. \tag{41}$$

Combining Eqs. (40)–(41) and the linear characteristic of inner product, the totality of each source contribution proportions at the jth observation point is

$$\sum_{i=1}^{N} \mathrm{CP}_{ij} = \sum_{i=1}^{N} \frac{\hat{y}_{ij} \cdot x_j}{x_j \cdot x_j} = \frac{x_j \sum_{i=1}^{N} \hat{y}_{ij}}{x_j \cdot x_j} = \frac{x_j \cdot x_j}{x_j \cdot x_j} = 100\%. \tag{42}$$

The sum of contribution proportions is 1, which indicates that the obtained CP can truly and quantitatively evaluate the relative influence of each source in the mixed signals.

But for the energy-based contribution evaluation does not always meet $x_j^2 = \sum_{i=1}^{N} \hat{y}_{ij}^2$, so $\sum_{i=1}^{N} \hat{y}_{ij}^2 \Big/ x_j^2$ is not always equal to 1, indicating that the obtained contribution by the energy-based contribution quantification can't truly express the relative impact from each source.

It should be noted that Eq. (40) is the case of one direction. For the case of multi-directional vibration such as the vibration in X-direction, Y-direction and Z-direction, the source contributions in each direction need to be obtained respectively, and then the overall CP of the ith source to x_j is calculated as follows:

$$\mathrm{CP}_{ij} = \frac{(\hat{y}_{ij})_X \cdot (x_j)_X + (\hat{y}_{ij})_Y \cdot (x_j)_Y + (\hat{y}_{ij})_Z \cdot (x_j)_Z}{(x_j)_X \cdot (x_j)_X + (x_j)_Y \cdot (x_j)_Y + (x_j)_Z \cdot (x_j)_Z}, \tag{43}$$

where $()_x$, $()_y$ and $()_z$ represent the signal in X-, Y- and Z-direction, respectively.

4 Simulations Analysis

4.1 Superiority of the RBCBD Algorithm

The following comparison algorithms are taken to verify the superiority of the RBCBD algorithm. Algorithm A: The contrast function is the normalized reference-based quadratic contrast function and its optimization method is the adaptive step optimization method; Algorithm B: The reference-based cubic contrast function and the fixed step optimization method; Algorithm C: The classical fourth-order cumulant contrast function and the adaptive step optimization method.

The types of the source signals are set as below: $s_1(t)$ is a sinusoidal wave; $s_2(t)$ and $s_3(t)$ are multi-component signals. The generated source signals follow the form of these functions:

$$\mathbf{s}(t) = \begin{bmatrix} s_1(t) \\ s_2(t) \\ s_3(t) \end{bmatrix} = \begin{bmatrix} \sin\left(2\pi f_1 t\right) \\ 0.69\sin\left(2\pi f_2 t\right) + 0.55\sin\left(4\pi f_2 t\right) + 0.47\sin\left(6\pi f_2 t\right) \\ 0.79\sin\left(2\pi f_3 t\right) + 0.48\sin\left(4\pi f_3 t\right) + 0.38\sin\left(6\pi f_3 t\right) \end{bmatrix}, \tag{44}$$

where f_1, f_2, f_3 and the signal phases are generated stochastically. The sampling frequency is 1024 Hz. The entire sampling time is 1 s. The filtering order of the randomly generated mixing filter $\boldsymbol{A}$ is 10. 25 dB white noise is added to the model shown in Eq. (1) to obtain the mixed signal $\boldsymbol{x}$.

The source extraction performance is measured by the global filter error index in Ref. [26], which is defined as:

$$e_{\boldsymbol{g}} \triangleq 1 - \frac{\max\limits_{i\in\{1,\cdots,N\}} \left\|g_i\right\|_i^2}{\sum\limits_{i\in\{1,\cdots,N\}} \left\|g_i\right\|_i^2}. \tag{45}$$

The value range of the error index is [0, 1]. And the closer this error index is to 0, the better the extraction performance is.

4.1.1 Selection of the Iterative Number of the Reference Signal

This section explores the influence of the iterative number of the reference signal l_{rs} on extraction performance. The source signals are generated by the functions in Eq. (44). The mixed signals $\boldsymbol{x}$ obtained by $\boldsymbol{x}=\boldsymbol{A}^*\boldsymbol{s}$ are processed by the proposed algorithm with different l_{rs}. The first mixed signal x_1 is selected as the reference signal.

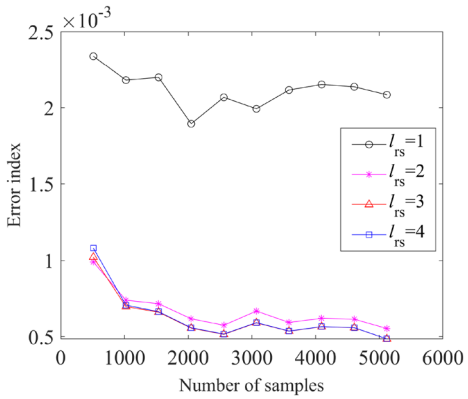

Figure 2 Extraction performance of RBCBD algorithm with different l_{rs}

The algorithm parameters are set as follows: The maximum iteration number is 50000; the separation filter order D is 10; the convergence threshold is 10^{-6}. The average $e_{\boldsymbol{g}}$ of 20 random runs is brought to evaluate the extraction performance. In each run, the coefficients of $\boldsymbol{A}$ and the phases of each source are regenerated stochastically. Figure 2 demonstrates the error index of different iterative number l_{rs} with the increase of the number of samples N_e.

As can be seen from Figure 2, the extraction performance will not be significantly improved with the increase of l_{rs} under the condition of $l_{\mathrm{rs}}>3$. Therefore, in

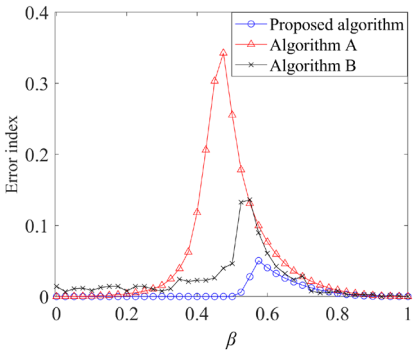

Figure 3 Separation performance versus β by the proposed algorithm and the comparison algorithms

the next simulations and experiments, l_{rs} are set to 3 both in the RBCBD algorithm and the algorithm A and B.

4.1.2 Effect of the Reference Signal

This section explores the effect of the reference signal and compares the proposed algorithm with algorithm A and algorithm B. We choose $r(n) = \beta s_1(n) + (1-\beta)s_2(n)$ with $\beta \in [0, 1]$ as the reference signal. The proposed RBCBD algorithm and the comparison algorithms are taken to deal with the mixed signals respectively. The e_g of the three algorithms is drawn versus β in Figure 3 where each e_g is the average of 20 runs. The three algorithms use the same parameter settings: The maximum iteration number is 50000; the separation filter order D is 10; the convergence threshold is 10^{-6}.

As shown in Figure 3, better results of the three algorithms are all obtained when β is near to 0 or 1. With β near to 0.5, algorithm A fails to extract, while the proposed algorithm still works well. Since the adaptive step optimization method is adopted in the proposed algorithm, the oscillation near the convergence point can be effectively eliminated, reducing the steady-state error. Therefore, the proposed algorithm has higher separation accuracy than algorithm B with fixed step size. These results verify that the proposed algorithm is a more robust algorithm. The satisfying result can still be obtained by RBCBD algorithm even with the inaccurate reference signal, which illustrates that the proposed RBCBD algorithm is less sensitive to the reference signal. This provides great convenience for the construction of the reference signal and improves the feasibility of the algorithm in practical application.

4.1.3 Comparison in Extraction Accuracy

To analyze the extraction performance in noisy situations, RBCBD algorithm and the comparison algorithms are adopted to deal with the mixed signals $\boldsymbol{x}$ with noise. The average e_g of the four algorithms is drawn versus the signal-to-noise ratio (SNR) of the added noise in Figure 4 where each e_g is the average of 20 runs.

As can be perceived from Figure 4, the algorithms with reference is superior to algorithm C without reference in extraction accuracy, indicating that the introduction of the reference signal can improve the extraction accuracy. The algorithm A with accurate reference signals also has high separation accuracy. However, algorithm B has lower separation accuracy than the proposed algorithm and algorithm A due to the influence of steady-state error.

4.1.4 Comparison on Extraction Efficiency

To compare the extraction efficiency, the RBCBD algorithm and comparison algorithms are taken to deal with the mixtures $\boldsymbol{x}$ with 25 dB noise. The number of iterations is drawn versus the number of samples in Figure 5 where each number of iterations is the average of 20 runs. The running time of the four algorithms is drawn versus the number of samples in Figure 6 where each running time is the average of 20 runs.

As can be perceived in Figures 5 and 6, the RBCBD algorithm with the adaptive step optimization is superior

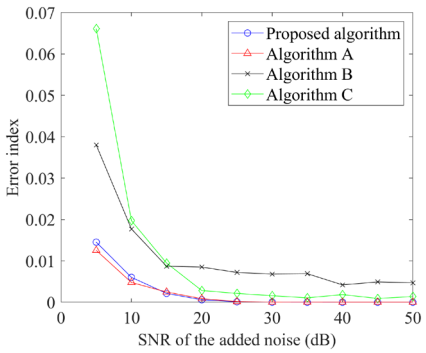

Figure 4 Extraction performance of the four algorithms in the case of noise

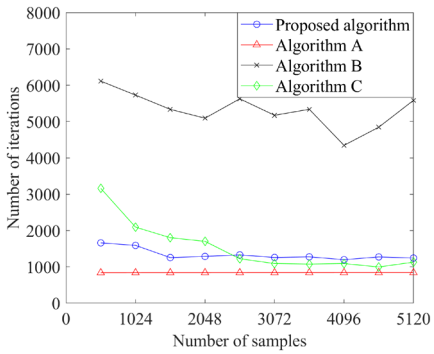

Figure 5 Iterations comparison of the algorithms

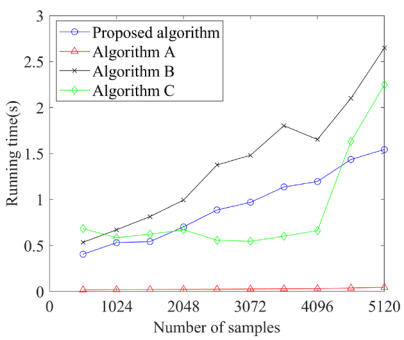

Figure 6 Running time comparison of the algorithms

to algorithm B with the fixed step optimization in efficiency, indicating that the adaptive step optimization can significantly improve the efficiency. It should be noted that the suitable value 0.01 is selected for the step size of algorithm B in this comparison through the attempt of different values in advance. A smaller step size will lead to the slower convergence, while a bigger step size will result in difficult convergence due to the larger steady-state error. Therefore, the efficiency advantage of the RBCBD algorithm will be more obvious in practical applications where there is no prior information for a suitable step size.

However, the extraction efficiency of the proposed algorithm is lower than that of the quadratic algorithm A with the adaptive step optimization. Compared with algorithm C, which also adopts the adaptive step optimization, the proposed algorithm does not show obvious efficiency advantage. The computational complexity in each iteration of the proposed cubic algorithm is greater than that of the quadratic algorithm, magnifying the advantage of algorithm A in running time. Therefore, the improvement of the reference-based cubic algorithm in terms of separation accuracy and robustness on the reference signals is at the cost of reducing the efficiency, while the proposed algorithm relieves the efficiency problem by the adaptive step optimization.

To sum up, through the above comparisons, the proposed method has the following superiorities. The extraction accuracy is improved by introducing reference signal. The proposed algorithm is more robust to the reference signal selection. The proposed algorithm improves the efficiency by the adaptive step size gradient optimization.

4.2 Validation of the Source Quantitative Identification

The frequencies f_1, f_2 and f_3 in Eq. (44) used to generate the sources are set to 70 Hz, 80 Hz and 50 Hz respectively. The phases of the corresponding sources are generated stochastically. The temporal waveforms and frequency spectrums of simulation sources are displayed in Figure 7. The mixed signals as shown in Figure 8 are obtained by $\boldsymbol{x}=\boldsymbol{A}^*\boldsymbol{s}$ and adding an additional 25 dB noise. The mixed signals are handled with the proposed RBCBD algorithm, and the extracted source signals are presented in Figure 9. The error indexes e_g of each extracted signal are 8.41×10^{-4}, 2.78×10^{-4}, and 4.37×10^{-4}, respectively, indicating that the successful source extraction has been achieved by the RBCBD algorithm.

Then the CP of each source to different observed signals is worked out by the contribution evaluation method presented in Eq. (40), so as to achieve the quantitative identification of sources.

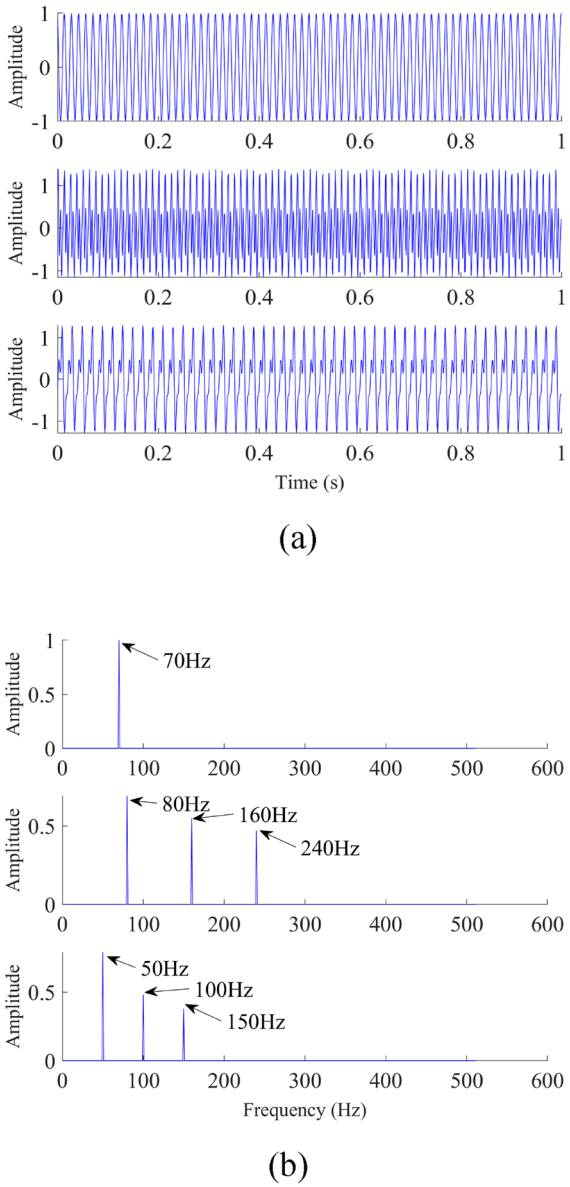

Figure 7 Simulation source signals $\boldsymbol{s}$: **a** Temporal waveforms, **b** Frequency spectrums

The true source contributions can be calculated by the known $\boldsymbol{s}$ and $\boldsymbol{A}$, and then the true CP can be obtained. Figure 10 lists both the calculated CP and the true one. It is obvious that the calculated CP are very close to the true CP. The mean error is 0.51% and the maximum is only 1.07%. The results firmly verified the availability of the source quantitative identification method.

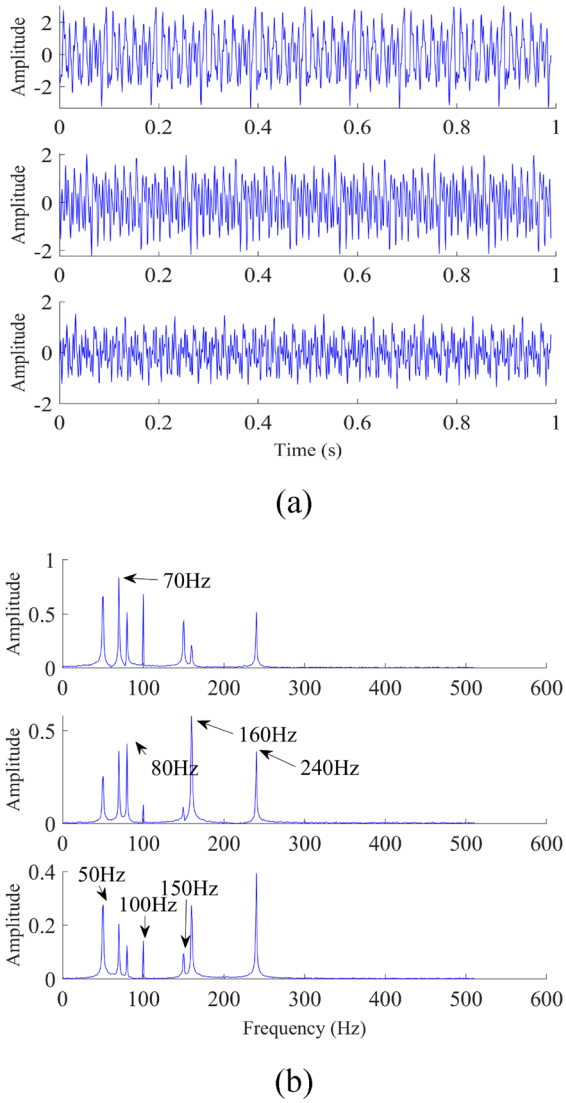

Figure 8 Simulation mixed signals ***x***: **a** Temporal waveforms, **b** Frequency spectrums

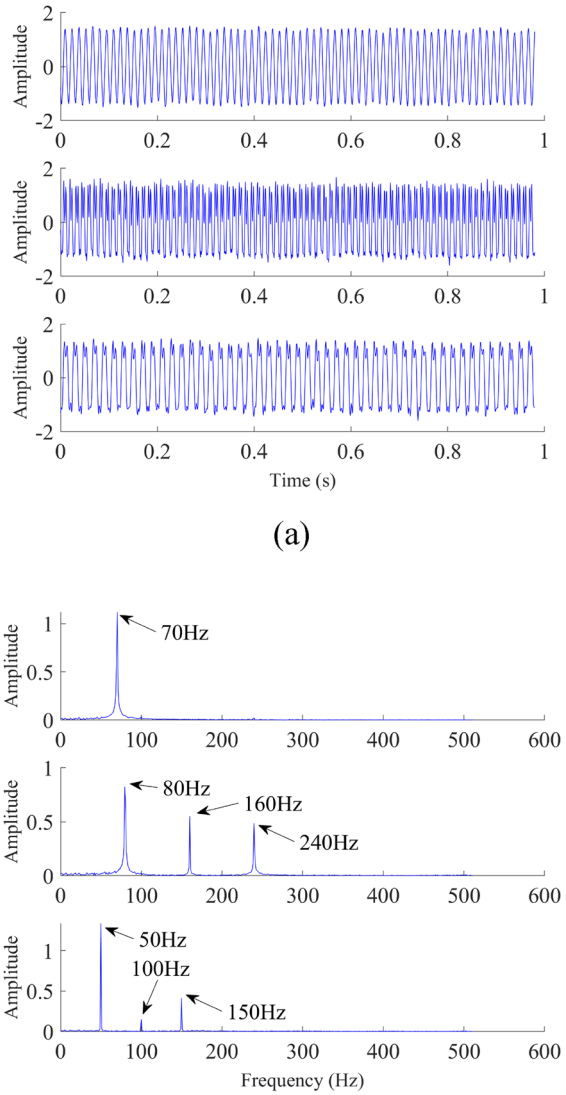

Figure 9 Simulation extracted signals ***y***: **a** Temporal waveforms, **b** Frequency spectrums

5 Experimental Verification

Further test is given by the vibration experiment of simulated satellite of aluminum honeycomb structure. Next, satellite ground experiment is carried out to prove the validity of the proposed method in the quantitative identification of the satellite micro-vibration sources.

5.1 Simulated Satellite Experiment

In this section, we conducted the excitation experiment on a simulated satellite to further verify the availability of this method.

5.1.1 Experimental Setup

An experimental device simulating the actual satellite structure was manufactured, and the excitation experiment was carried out. The overall experimental system is exhibited in Figure 11.

The experimental model is made of the aluminum honeycomb sandwich plate, and the plates are connected by embedded bolts. The manufacturing materials and the connection form widely appear in actual

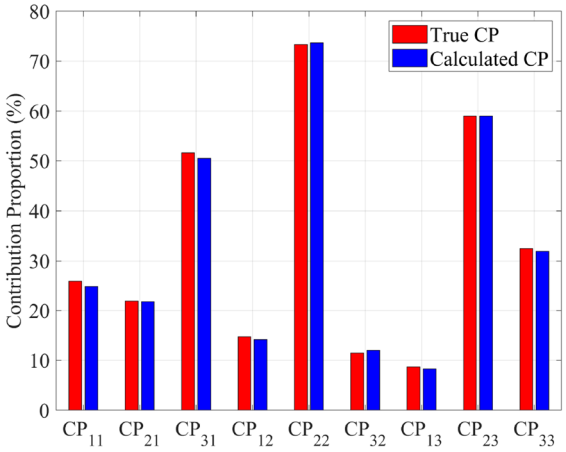

Figure 10 Results of the quantitative identification using the RBCBD algorithm in simulations analysis

satellites. The model is divided into upper and lower cabins to simulate the payload and propulsion cabin respectively. The camera is simulated by an aluminum column structure, which is arranged on the top.

The model was lifted on the steel tubes bracket by the elastic slings to isolate the ground vibration. Motors and vibration exciters for generating four experimental source signals were arranged around the lower cabin. The experimental model is shown in Figure 11a.

The experimental control instruments shown in Figure 11b were placed in another room to isolate the self-generated noise, where HBM DAS recorded the vibration signals measured by PCB356b18 accelerometers. The vibration exciters were controlled through power amplifier and signal generator, and the motors were controlled through the speed controllers to obtain the desired source signals.

The arrangement of the accelerometers is shown in Figure 11c. The accelerometers 1 and 2 were respectively arranged on the top and bottom of the camera simulator, and the accelerometers 3 and 4 were arranged on the surface of the experimental model.

5.1.2 Experimental Validation

The experimental source signals were measured by those accelerometers placed near each motor or vibration exciter when each source operates separately. The temporal waveforms and frequency spectrums of the experimental source signals are displayed in Figure 12, where the first two signals are the source signals of the exciters and the other two are those of the motors. The sampling frequency was 5000 Hz. The entire sampling time

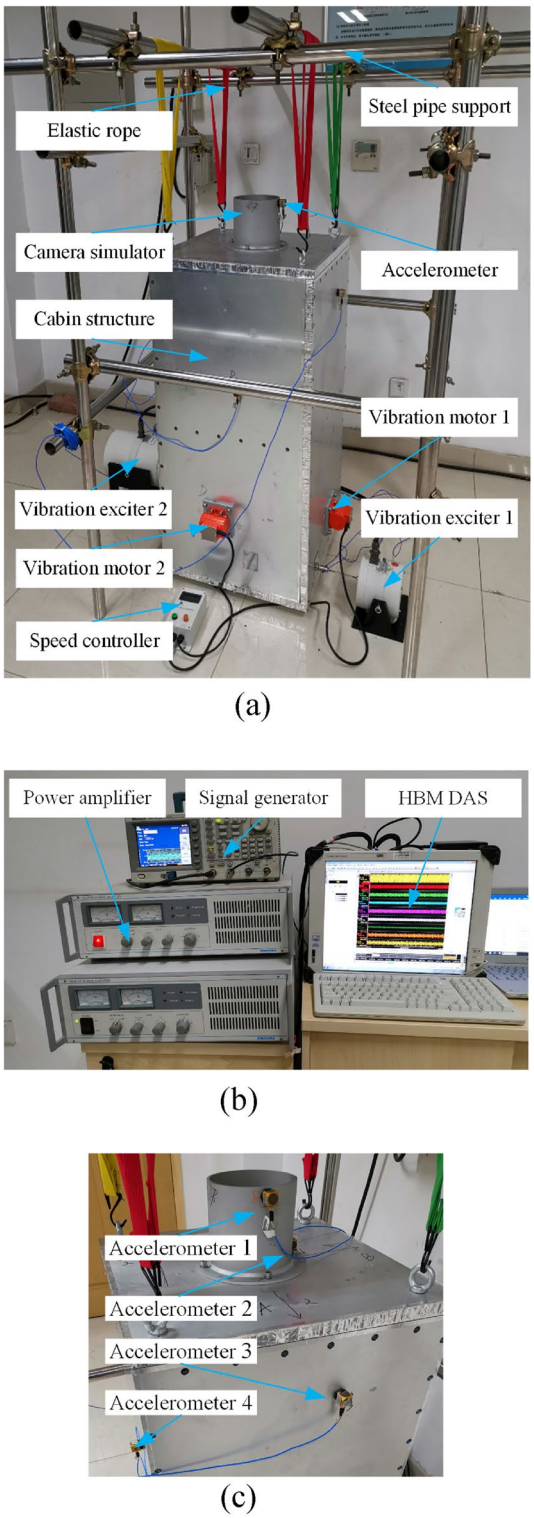

Figure 11 Simulated satellite experiment system: **a** Simulated cabin structure, **b** Experimental control instruments, **c** Arrangement of the accelerometers

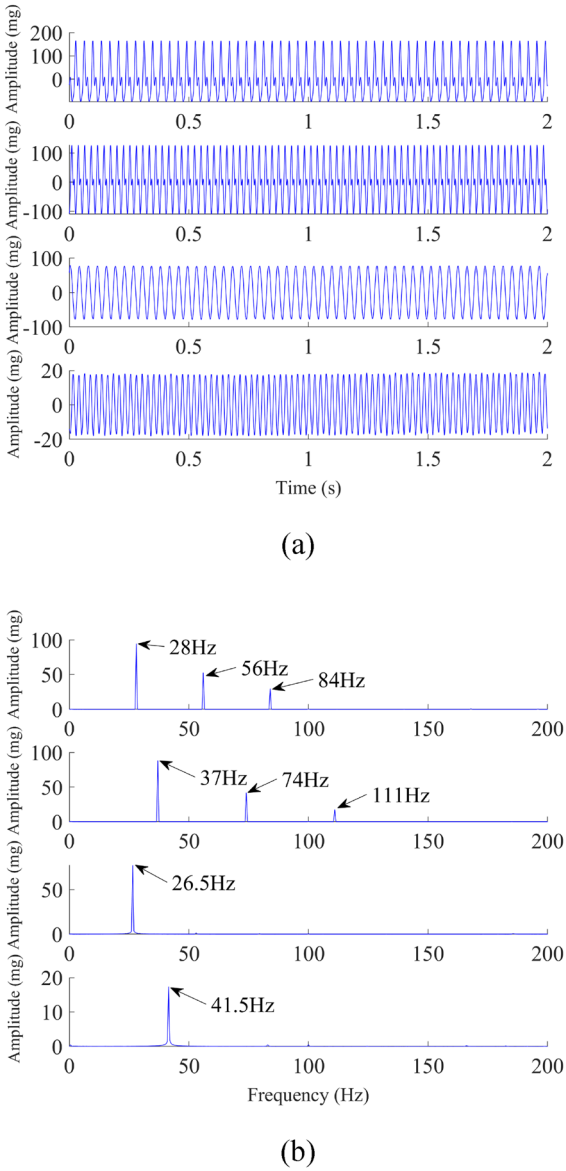

Figure 12 Experimental source signals: **a** Temporal waveforms, **b** Frequency spectrums

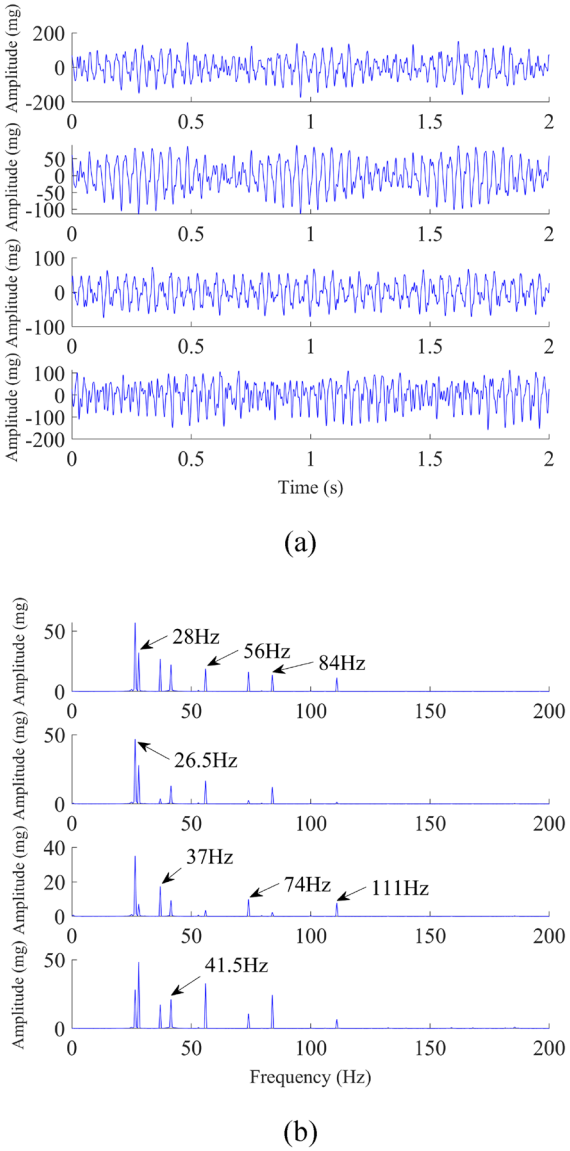

Figure 13 Experimental mixed signals: **a** Temporal waveforms, **b** Frequency spectrums

were 2 s. The subsequent spectrums only give the part of 0–200 Hz to visually display the detailed characteristics. The collected experimental mixed signals when all sources work simultaneously are presented in Figure 13.

The RBCBD algorithm was brought to process experimental mixed signals and realized source extraction. The parameter settings were as follows: The maximum iteration number was 5000; the separation filter order D was 15; the convergence threshold was 10^{-7}; the iterative number of the reference signal l_{rs} was 3. The nonlinear mode decomposition method [32–34] was adopted to deal with the mixed signals, from which the harmonics were extracted to be the reference signals. It can be seen from Section 4.1.2, the reference signals do not need to be very accurate, so the reference signals constructed by nonlinear mode decomposition can meet the requirements. Figure 14 exhibits the experimental extracted signals. It can be drawn from the comparison between Figure 12 and Figure 14 that the frequency composition and temporal waveform of the extracted signals are basically identical with those of the source signals. It can be considered that each extracted signal is a filtering of the corresponding source signal, so the experimental source extraction has been successfully achieved.

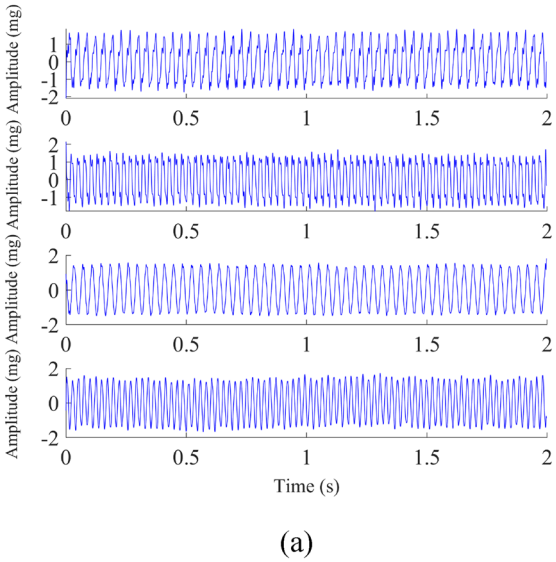

Figure 14 Experimental extracted signals: **a** Temporal waveforms, **b** Frequency spectrums

Table 1 Contribution calculation results of the model experiment

	S_1	S_2	S_3	S_4	Average
True CP (%)	22.92	18.00	51.47	7.62	–
Calculated CP (%)	24.87	15.51	51.42	8.07	–
Error (%)	1.96	2.49	0.05	0.45	1.24

Then, the contribution quantification was implemented to evaluate the contributions of the sources. The micro-vibration at camera position is an important factor to the decline of observation satellite resolution, so we are concerned with the vibration of the camera simulator. Therefore, the CP of each source to the measuring position 1 needs to be calculated. When each source worked separately, the true contribution of each source at measuring position 1 was the signal measured by accelerometer 1, and then the true CP could be obtained. Table 1 lists both the calculated and true CP. The errors of the calculated CP are 1.96%, 2.49%, 0.05% and 0.45%, and the mean error is 1.24%.

The satisfactory results of this simulated satellite experiment demonstrate that the proposed method can successfully extract each source from the experimental mixtures and accurately evaluate the vibration effect of each source to the camera simulator. The availability of the proposed method is further confirmed.

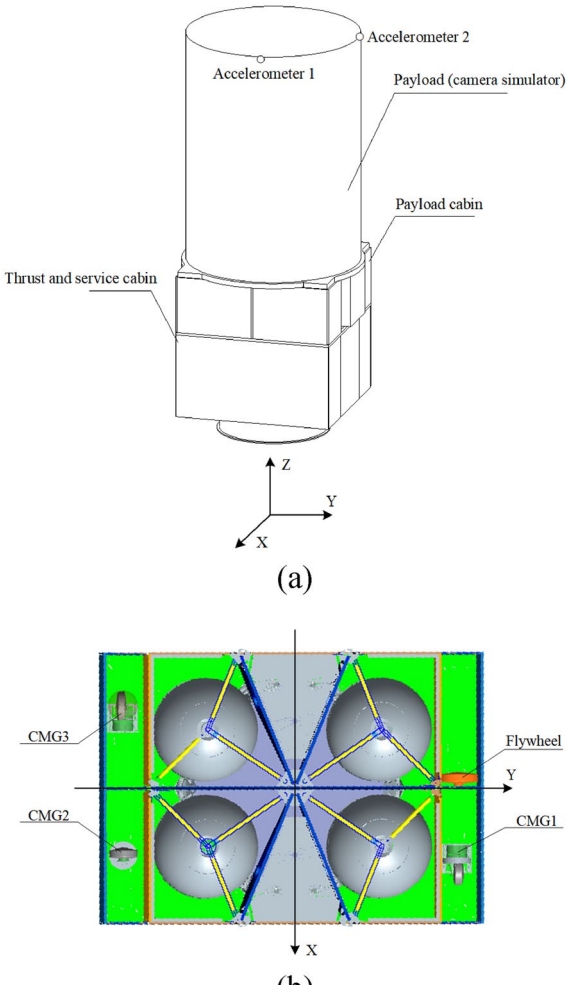

Figure 15 Diagram of the experiment satellite: **a** Construction of experiment satellite, **b** Layout of the micro-vibration sources

5.2 Satellite Ground Experiment

For the feasibility test in the satellite micro-vibration source identification, this method was applied to satellite ground experiment to extract the signals of control moment gyroscope and flywheel and to calculate the contribution proportions of vibration sources to the sensitive load area.

5.2.1 Introduction to the Experiment System

The experiment satellite was composed of three parts: The thrust and service cabin, payload cabin and payload, as shown in Figure 15a. The micro-vibration sources, including one flywheel and three control moment gyroscopes (CMG 1, CMG 2 and CMG 3), were installed in the small cabins around the thrust and service cabin, as shown in Figure 15b. All instruments and equipment in the cabins were simulated by the counterweight, the weight of which was consistent with the design state. A camera simulator was used as the payload. The accelerometers were arranged on the top of the camera simulator, where was the sensitive load area.

5.2.2 Experimental Verification

Take a certain working condition as an example, in which CMG1 operated with the high-speed shaft at 6000 r/min and low-speed shaft locked and flywheel operated at 800 r/min. By analyzing the vibration signals measured by the accelerometers, it can be found that the vibration of the measuring point 2 is greater than that of the measuring point 1. Therefore, we are mainly concerned with the vibration of the measuring point 2 and each source contribution to measuring point 2 needs to be calculated.

Firstly, we dealt with the vibrations in *X*-direction. Similarly, when each source ran separately, the experimental source signals were collected. The waveforms of the signals are very complex but the Fourier spectrums are more intuitive, so only the Fourier spectrums are displayed, as shown in Figure 16, where the first signal is from the control moment gyroscope and the second signal is from the flywheel. The sampling was kept for 2 s and the sampling frequency was 6400 Hz. The 0–1000 Hz part of the signal spectrum is exhibited to show the signal characteristics in detail. When both sources were running, the first mixed signal in Figure 17 was collected by accelerometer 1 and the second by accelerometer 2.

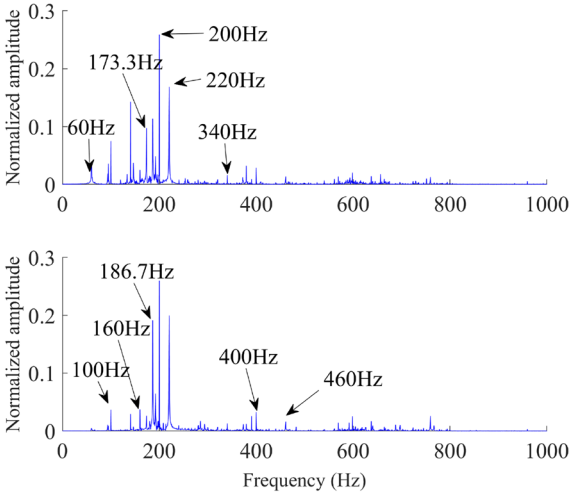

Figure 17 Spectrums of *X*-direction mixed signals

The RBCBD algorithm was carried out to extract the source signals of ground experiment. The nonlinear mode decomposition was taken to extract harmonics signals from the observation signal of measure point 2 in

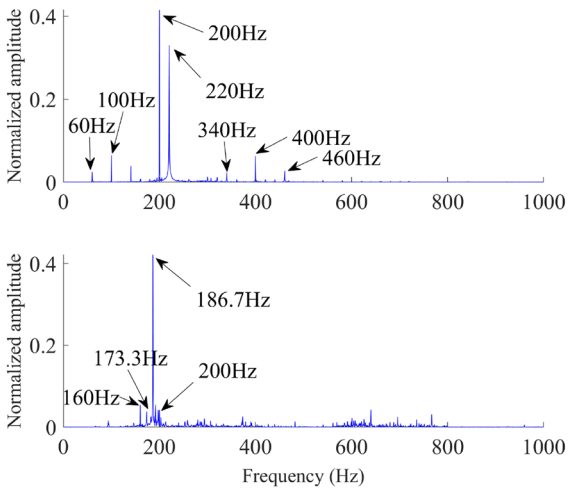

Figure 16 Spectrums of *X*-direction source signals

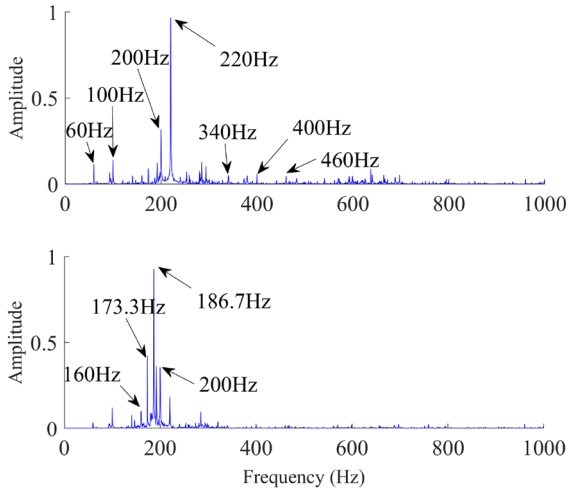

Figure 18 Spectrums of *X*-direction separated signals

Table 2 Contribution calculation results of the satellite experiment

	CMG	Flywheel	Average
True CP in *X*-direction (%)	70.16	29.84	–
Calculated CP in *X*-direction (%)	62.40	30.92	–
True CP in *Y*-direction (%)	70.87	29.13	–
Calculated CP in *Y*-direction (%)	78.75	24.29	–
True CP in *Z*-direction (%)	39.02	60.98	–
Calculated CP in *Z*-direction (%)	34.14	65.11	–
True overall CP (%)	69.72	30.28	–
Calculated overall CP (%)	68.13	29.19	–
Error (%)	1.59	1.09	1.34

the *X*-direction as the reference signals. The maximum iteration number was 5000; the separation filter order D was 45; the convergence threshold was 10^{-7}; the iterative number of the reference signal l_{rs} was 3. The frequency components of the extracted signals are displayed in Figure 18. Consistent frequency components can be discovered between Figure 16 and Figure 18, indicating that the extraction of the vibration source signals is successfully achieved.

Then, the same steps were taken to process the *Y*-direction and *Z*-direction mixtures respectively to extract source signals and source contributions.

Finally, the CP of each micro-vibration source at measuring point 2 was calculated using the proposed contribution evaluation method, so as to accomplish the source quantitative identification. True contribution proportions were obtained by the true source contributions. Both the calculated contribution proportions and true contribution proportions are presented in Table 2. The errors of the calculated contribution proportions are 1.59% and 1.09%, and the average error is 1.34%, which meets the error requirements in engineering application. Satisfactory results have been obtained in the quantitative identification of the satellite micro-vibration sources.

6 Conclusions

In conclusion, the method proposed in this paper can effectively achieve the quantitative identification of the satellite micro-vibration sources, so as to provide the basis for suppressing the satellite micro-vibration.

(1) In this paper, aimed at the source quantitative identification, the source extraction and contribution evaluation are studied. To accurately and efficiently extract the sources, a semi-blind deconvolution algorithm is proposed. We first propose the normalized reference-based cubic contrast function and theoretically prove its validity. The cubic contrast function enhances the extraction accuracy and the robustness of the algorithm. After that, by deriving the optimal step size of gradient iteration under the new contrast function, we propose the adaptive step size gradient optimization method, which improves the efficiency. Besides, by introducing the reference signal iterative updating and the deflation procedure, the accuracy of the algorithm is further improved. Furthermore, the contribution evaluation method based on vector projection is presented to realize the high-accuracy source contribution evaluation.

(2) Numerical simulation is constructed as the first test to authenticate the effectiveness of this method. Simulation results reveal that this method has the ability to extract simulated sources from convolution mixtures and accurately evaluate source contribution with error of less than 1.5%. Compared with other algorithms, the RBCBD algorithm is advantageous in terms of the accuracy, robustness and efficiency. Then in the simulated satellite experiment, experimental source quantitative identification is accurately realized with error of less than 3%, which further confirmed the availability.

(3) The method was also applied to the satellite ground experiment. The signals of CMG and flywheel were extracted respectively, and the contribution calculation of the vibration sources to the sensitive load area was successfully realized with average error 1.34%.

Acknowledgements
Not applicable.

Authors' Contributions
XL was in charge of the whole trial; XL wrote the manuscript; TG and YL assisted with sampling and laboratory analyses. All authors read and approved the final manuscript.

Author's Information
Xin Luo born in 1995, is currently a PhD candidate at *State Key Laboratory for Manufacturing Systems Engineering, Xi'an Jiaotong University, China*. She received her bachelor degree from *Chang'an University, China,* in 2017. Her research interests include blind source separation, intelligent diagnosis and condition monitoring.

Zhousuo Zhang born in 1964, is currently a professor at *Xi'an Jiaotong University, China*. He received his PhD degree from *Xi'an Jiaotong University, China,* in 2004. His research interests include condition monitoring, fault diagnosis and life prediction of mechanical equipment.

Teng Gong born in 1990. He received his PhD degree from *Xi'an Jiaotong University, China*, in 2021. His research interests include blind source separation, intelligent diagnosis and condition monitoring.

Yongjie Li born in 1996. He received his master degree from *Xi'an Jiaotong University, China*, in 2022. His research interests include blind source separation, intelligent diagnosis and condition monitoring.

Funding
Supported by National Natural Science Foundation of China (Grant No. 51775410), and Science Challenge Project of China (Grant No. TZ2018007).

Data Availability
The data that has been used in this paper is confidential.

Declarations

Competing Interests
The authors declare that they have no competing interests.

Received: 19 April 2022 Revised: 25 July 2023 Accepted: 27 July 2023
Published online: 30 August 2023

References

[1] Q P Cao, Y C Li, X J Dong, et al. Influence of satellite micro-vibrationon signal-to-noise ratio of wind lidar. *Laser & Optoelectronics Progress*, 2020, 57(9): 092802.
[2] A Mankour, A Smahat, R Guy, et al. Experimental investigation of micro-vibrations induced by reaction wheels on earth observation satellite. *Advances in Space Research: The Official Journal of the Committee on Space Research(COSPAR)*, 2021, 68(11): 4484-4495.
[3] Y F Guo, Z Z Zhang, T Gong, et al. Generalized variational mode decomposition for interlayer slipping detection of viscoelastic sandwich cylindrical structures. *Measurement Science and Technology*, 2018, 29(9): 095001.
[4] D Xie, S Hong, C Yao. Optimized variational mode decomposition and permutation entropy with their application in feature extraction of ship-radiated noise. *Entropy*, 2021, 23(5): 503.
[5] Y Shao, C Miao, B Li, et al. Simultaneous de-noising and enhancement method for long-span bridges health monitoring data based on empirical mode decomposition and fractal conservation law. *Measurement Science and Technology*, 2019, 30(6): 065103.
[6] G Cheng, X Z Wang, Y R He. Remaining useful life and state of health prediction for lithium batteries based on empirical mode decomposition and a long and short memory neural network. *Energy*, 2021, 232: 121022.
[7] Y Zhang, X Du, G Wen, et al. An adaptive method based on fractional empirical wavelet transform and its application in rotating machinery fault diagnosis. *Measurement Science and Technology*, 2019, 30(3): 035005.
[8] H Wijaya, P Rajeev, E Gad, et al. Distributed optical fibre sensor for condition monitoring of mining conveyor using wavelet transform and artificial neural network. *Structural Control and Health Monitoring*, 2021, 28(11): e2827.
[9] H F Wu, D Li, M Z Lu, et al. FMRI activations via low-complexity second-order inverse-sparse-transform blind separation. *Digital Signal Processing*, 2021: 103137.
[10] S Akhavan, H Soltanian-Zadeh. Blind separation of sparse sources from nonlinear mixtures. *Digital Signal Processing*, 2021, 118: 103220.
[11] F A Pereira, S F Silva, I N Santos. Blind source separation methods applied to evaluate harmonic contribution. *International Transactions on Electrical Energy Systems*, 2021, 31(12): e13149.
[12] D Blacodon, A Mohammad-Djafari. Separation of acoustical source power spectral densities with bayesian sparsity enforcing. *Journal of Sound and Vibration*, 2020, 480: 115334.
[13] D Lukas, H U Reinhold. Integration of neural networks and probabilistic spatial models for acoustic blind source separation. *IEEE Journal of Selected Topics in Signal Processing*, 2019, 13(4): 815-826..
[14] C Stergiadis, V D Kostaridou, M A Klados. Which BSS method separates better the EEG signals? A comparison of five different algorithms. *Biomedical Signal Processing and Control*, 2022, 72: 103292.
[15] R S Kamathe, K R Joshi. A novel method based on independent component analysis for brain MR image tissue classification into CSF, WM and GM for atrophy detection in Alzheimer's disease. *Biomedical Signal Processing and Control*, 2018, 40: 41-48..
[16] Y Jia, P Xu. Convolutive blind source separation for communication signals based on the sliding Z-transform. *IEEE Access*, 2020, 8: 41213-41219.
[17] J Miettinen, E Nitzan, S A Vorobyov, et al. Graph signal processing meets blind source separation. *IEEE Transactions on Signal Processing*, 2021, 69: 2585–2599.
[18] X Zhao, Q Liu, J Li, et al. Blind source separation for face image based on deep leaming. *Proceedings of the IEEE International Conference on Automation, Electronics and Electrical Engineering*, Shenyang, China, November 16–18, 2018: 83–86.
[19] W Cheng, Z Z Jia, X F Chen, et al. Convolutive blind source separation in frequency domain with kurtosis maximization by modified conjugate gradient. *Mechanical Systems and Signal Processing*, 2019, 134: 106331.
[20] J T Lu, W Cheng, Y P Chu, et al. Post-nonlinear blind source separation with kurtosis constraints using augmented Lagrangian particle swarm optimization and its application to mechanical systems. *Journal of Vibration and Control*, 2019, 25(16): 2246-2260.
[21] J Thomas, Y Deville, S Hosseini. Time-domain fast fixed-point algorithms for convolutive ICA. *IEEE Signal Processing Letters*, 2006, 13(4): 228-231.
[22] C Simon, P Loubaton, C Jutten, et al. Separation of a class of convolutive mixtures: a contrast function approach. *Proceedings of the IEEE International Conference*, Phoenix, USA, March, 1999: 883-887.
[23] M Castella, S Rhioui, E Moreau, et al. Quadratic higher order criteria for iterative blind separation of a MIMO convolutive mixture of sources. *IEEE Transactions on Signal Processing*, 2006, 55(5): 218-232.
[24] M Castella, E Moreau. A new optimization method for reference-based quadratic contrast functions in a deflation scenario. *Proceedings of the IEEE International Conference on Acoustics, Speech and Signal Processing*, Taipei, China, April 19-24. 2009: 3161-3164.
[25] M Castella, E Moreau. New kurtosis optimization schemes for MISO equalization. *IEEE Transactions on Signal Processing*, 2012, 60(3): 1319-1330.
[26] R Dubroca, C D Luigi, M Castella, et al. A general algebraic algorithm for blind extraction of one source in a MIMO convolutive mixture. *IEEE Transactions on Signal Processing*, 2010, 58(5): 2484-2493.
[27] F Brahim, R Dubroca, C D Luigi, et al. Gradient algorithm for reference-based cubic contrast function in a deflation scenario. *Proceedings of the IEEE Statistical Signal Processing Workshop*, Nice, France, June 28-30, 2011: 293-296.
[28] X Luo, Z S Zhang, T Gong, et al. Adaptive step size EASI algorithm based on nonlinear correlation for on-line separation of satellite micro-vibration sources. *Measurement Science & Technology*, 2021(12): 32.
[29] P Loubaton, P A Regalia. Blind deconvolution of multivariate signals: A deflation approach. *Proceedings of the IEEE International Conference on Communications*, Geneva, Switzerland, May 23-26, 1993: 1160-1164.
[30] W Cheng, Z Zhang, S Lee, et al. Source contribution evaluation of mechanical vibration signals via enhanced independent component analysis. *Journal of Manufacturing Science and Engineering*, 2012, 134(2): 021014.
[31] J Zhang, Z Z Zhang, W Cheng, et al. Kurtosis-based constrained independent component analysis and its application on source contribution quantitative estimation. *IEEE Transactions on Instrumentation and Measurement*, 2014, 63(7): 1842-1854.
[32] M H Xiao, K Wen, C Y Zhang, et al. Research on fault feature extraction method of rolling bearing based on NMD and wavelet threshold denoising. *Shock and Vibration*, 2018, (7): 9495265.1 -9495265.11.
[33] J R Huerta-Rosales, D Granados-Lieberman, J P Amezquita-Sanchez, et al. Vibration signal processing-based detection of short-circuited turns in transformers: A nonlinear mode decomposition approach. *Mathematics*, 2020, 8: 575.
[34] H Demirezen, C E Erdem. Remote photoplethysmography using nonlinear mode decomposition. *Proceedings of the IEEE International Conference on Acoustics, Speech and Signal Processing(ICASSP)*, Calgary, Canada, April 15–20, 2018: 1060–1064.